University of Bristol - Explore Bristol Research
General rights
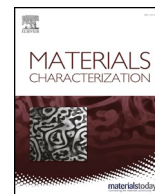
Preparation and analysis of strain-free uranium surfaces for electron and x-ray diffraction analysis

J.E. Sutcliffe[a,*], J.R. Petherbridge[b], T. Cartwright[b], R. Springell[a], T.B. Scott[a], J.E. Darnbrough[a]

[a] *Interface Analysis Centre, HH Wills Physics Laboratory, University of Bristol, Tyndall Avenue, Bristol, BS8 1TL, UK*
[b] *AWE, Aldermaston, Reading, Berkshire, RG7 4PR, UK*

ABSTRACT

This work describes a methodology for producing high quality metallic surfaces from uranium primarily for characterisation and investigations involving electron backscatter diffraction. Electrochemical measurements have been conducted to inform ideal polishing conditions to produce surfaces free from strain, induced by mechanical polishing. A commonly used solution for the electropolishing of uranium, consisting in part of phosphoric acid, was used to conduct the electrochemical experiments and polishing. X-ray diffraction techniques focusing on the surface show low stresses and strains are exhibited within the material. This is mirrored in good quality electron backscatter diffraction.

1. Introduction

Strong scattering of x-rays and electrons in atomically heavy (high-Z) materials greatly inhibits penetration and results in sampling of the near-surface region [1]. Therefore, excellent preparation of high-Z materials such as uranium is paramount for conventional, diffraction-based techniques. The susceptibility of the surface to mechanical deformation and chemical attack during preparation, leads to changes in chemistry and microstructural defects inhibiting coherent diffraction [2]. For the surface to be representative of the bulk, it is essential that artefacts arising from oxidation, work hardening, and preferential etching are removed.

Sequential mechanical and electrochemical polishing of uranium and its alloys is standard practice [3,4]. However, previous studies on uranium lack insight into the changes caused by this preparation method and how to perfect it. To develop and optimise the process, a consideration of the electrochemistry of electropolishing is required. Linear sweep and cyclic voltammetry were used to understand the kinetics of electron transfer and mass transport. Chronoamperometry (potential step voltammetry) was used to assess diffusional characteristics and conduct polishing. Electrochemical testing was ultimately carried out inform appropriate polishing potentials and durations.

Focused ion beam (FIB) milling procedures have been shown as particularly adept at producing surfaces capable of electron backscatter diffraction (EBSD) patterns in difficult to prepare materials such as uranium [5–10]. Additionally, FIB and EBSD combined on the same

instrument open the door to 3D reconstructions of the crystallographic microstructure [11,12]. However, ion beam damage is a natural consequence of these methods and has been reported to lead to phase transformations in steels [13]. FIB milling additionally introduces limits on the size of EBSD maps and location from which they may be collected.

This paper looks to elucidate the process of producing strain- and oxide-free surfaces in uranium metal through mechanical and electropolishing as characterised by x-ray diffraction (XRD) and EBSD. Strain-free surfaces allow interrogation of the bulk characteristics and are of interest for the assessment of microstructure, crystallographic texturing and corrosion properties.

2. Materials and techniques

2.1. Materials

Specimens used for this investigation were cast and rolled low carbon samples (~ 50 ppm) of depleted uranium (size: $10 \times 10 \times 0.75$ mm^3) provided by AWE plc. Specimens were subsequently cut to 3 10 × 0.75 mm³ to limit the number of original pieces used, ensuring homogeneity between samples.

2.2. Mechanical preparation

Samples were initially polished using SiC P360 grit paper to remove

---

gross oxide before being potted in Clarocit™ epoxy resin purchased from Buehler. Samples were subsequently polished with progressively finer papers from P180 through to P4000. This produces a topologically rough sample surface on the scale of electron microscopy, incapable of producing EBSD patterns.

Samples were ultrasonically cleaned in acetone and broken out of the resin. Samples were then rinsed in water, acetone and methanol to remove any grease and allowed to dry through evaporation. As specimens were prepared in a batch to increase uniformity, samples were subsequently placed under a (medium) vacuum to reduce oxygen contamination of the surface before electropolishing.

2.3. Electrochemistry configuration

Literature shows a bias for phosphoric acid-based solutions for uranium electropolishing with empirical evidence provided to prove their suitability [1,2,4,14,15]. For this work, a commonly used solution of 46% ethanol, 27% ethylene glycol and 27% phosphoric acid (85% assay) by volume [16], was selected to produce a strongly acidic electrolyte with a minimal presence of water or oxygen which would lead to anodisation of polished samples.

Electropolishing was carried out in a three-electrode cell, Fig. 1, utilising a Ag/AgCl reference electrode, a Pt wire as the counter electrode, and the sample as the working electrode. A Gamry 1000 potentiostat was used to conduct linear sweep, cyclic voltammetry and chronoamperometry experiments. Electropolishing was conducted under chronoamperometry conditions and the temperature was not controlled during the experiments.

A stirring rate of 900 rpm was achieved using a Fisher Scientific stirrer and a magnetic flea. All values of potential are quoted relative to the Ag/AgCl reference (+0.230 V vs the standard hydrogen electrode). Values of current have been normalised by each sample's exposed area to the solution to give a current density in mA/cm^2.

After electropolishing, all samples were rinsed with acetone, methanol and wiped using methanol-moistened blue-roll to remove any residue. For logistical considerations, all samples were studied by EBSD during the same electron microscope session. Samples were therefore returned to the (medium) vacuum to limit exposure to air and mitigate against deleterious surface oxidation.

2.4. Electron backscatter diffraction

SEM and EBSD was conducted on a Zeiss EVO MA10 scanning electron microscope fitted with a LaB$_6$ source, using a 20 μm aperture.
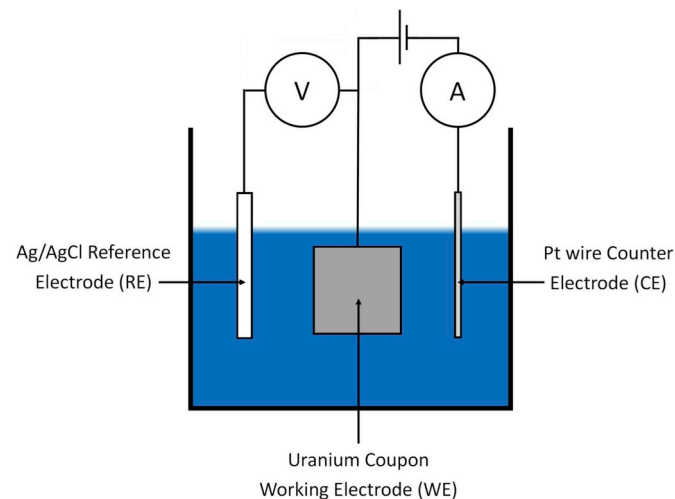

Fig. 1. Schematic of the experimental setup depicting the potentiostat acting as voltmeter, ammeter and supply.

A Digiview 3 high speed camera and EDAX OIM™ software were used to record and process EBSD data. Confidence indices (CI), the software's measure of the accuracy of a solution to the experimental Kikuchi pattern, were chosen as the predominant method of assessing EBSD pattern quality, due to the ability to easily compare datasets. CI values in excess of 0.1 have been shown to produce a sufficiently adequate representation of the crystallographic microstructure, particularly after post-processing cleaning routines [17]. Therefore, microscope and EBSD image processing settings were held fixed; 2 frames with an exposure time of 0.05 s were averaged for each scan point. The EBSD camera has a full resolution 1248 × 936 pixels but every map was collected with 4 × 4 binning resulting in an effective resolution of 312 × 234 pixels. All EBSD maps were run over areas sizing at least 100 μm × 50 μm. Image processing consisted of; background subtraction, dynamic background subtraction, normalised intensity histogram and median smoothing filter functions. With the exception of Fig. 7c, no clean-up routines have been applied to any maps featured.

2.5. X-ray diffraction

XRD scans were obtained using a Philips X'Pert Pro multipurpose diffractometer utilising an Empyrean Cu Kα radiation source. The x-ray tube was operated at 40 kV and 40 mA with 0.04 radian Soller slits and 1/2° divergence slits. High angle powder scans were performed over a range of 25 to 140°.

Stress and strain within the sample were determined by two complementary XRD techniques. Firstly, Williamson-Hall peak analysis was applied to the powder data to assess strain and coherent volume size [18]. This method considers the change in peak width as the scattering vector is extended into the material normal to the surface.

The $sin^2\psi$ method assessed residual stresses by measuring the same Bragg peak at different effective sample tilts, thus sweeping the (fixed length) scattering vector progressively closer to the surface. A complete description of the technique is provided by Welzel *et al.* [19]. The effective sampling depth, τ_ω, is given by the following equation,

$$\tau_\omega = \frac{sin^2\theta - sin^2\psi}{2\,\mu\,sin\theta\,cos\psi}$$

(1)

θ is half the diffraction angle (2θ), ψ is the angle between the original surface normal and the resultant surface normal following sample 'tilting', and μ is the absorption coefficient for x-rays. For an 8 keV Cu Kα source, the absorption coefficient in uranium is equal to 5760 cm^{-1} [20].

The (135) reflection, measured at a 2θ value of 131.5°, allowed for the greatest accessible value of $sin^2\psi$ (0.8). Therefore, using the previous formula, a minimum information depth of 67 nm was achieved. Since the *d* spacing of this peak is 0.845 Å, fewer than 800 planes were accessed in this configuration. In comparison, the specular configuration, i.e. $sin^2\psi = 0$, corresponds to greater than 9000 layers. Scans were performed over a range of 4° in 2θ with a step size of 0.02° and a counting time of 4 s per step. Positive tilts were used to avoid the beam footprint exceeding the size of the sample at high values of $sin^2\psi$.

For both analyses, peak fitting was undertaken using a least-squares fitting routine using the MATLAB Mfit package produced at the Institut Laue-Langevin [21]. Peaks were fitted with Pseudo-Voigt functions using doublet peaks with wavelengths of 1.54059 and 1.54432 Å. Peaks were modelled with the Kα$_1$ line exhibiting twice the intensity of the Kα$_2$ line.

Due to significant preferred orientation caused by extensive processing, precise lattice and structural parameters used in the generation of material files for EBSD analysis were obtained from full pattern XRD fitting using GSAS-II [22].
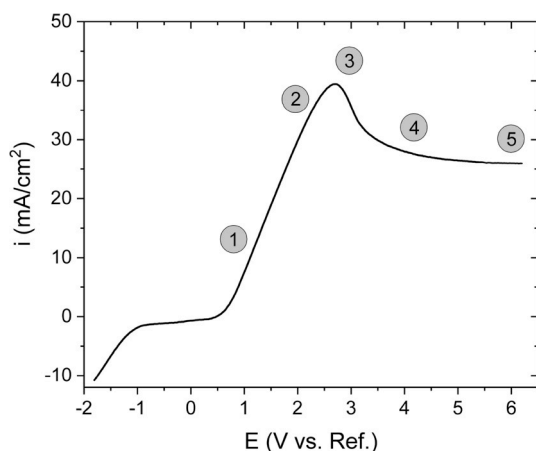
Fig. 2. Typical linear sweep curve showing the potentials used in the potential study labelled above the curve. Data taken for the linear sweep curve was obtained using a scan rate of 50 mV/s.

3. Results

3.1. I–V curve characteristics

Fig. 2 shows a typical single linear sweep starting in the cathodic region (-2 V) and finishing deep in the anodic region ($+6$ V). In the cathodic region, negative currents were experienced with bubbles observed to form readily on the surface of the working electrode. Linear sweep curves subsequently displayed an initial plateau, -1 to 0.5 V, producing no current. Further into the anodic region, a short exponential rise, region 1, occurred before an extended linear rise, region 2. Curves subsequently experienced a turning point, region 3. Between $+3$ V and $+5$ V, the current falls to a plateau, regions 4 and 5, limiting the current density to ~ 25 mA/cm^2. The plateau region is sustained to at least $+10$ V.

It would be expected that the current rises again as oxygen is evolved, however high acidity and an appreciable lack of water (and therefore OH^- ions) in the solution is thought to be precluding this reaction, pushing it to potentials greater than the capabilities of the potentiostat used.

Increasing scan rates were found to increase the total current generated as expected; higher scan rates produce a smaller diffusion layer permitting greater current. Additionally, the peak was observed to increase to higher potentials for higher scan rates indicating slow kinetics with respect to the experiment and irreversible reactions.

Cyclic voltammetry was performed to further examine the kinematics and electrochemical stability of the system. Between the first and second cycles, the current increases for anodic potentials. This can be attributed to the time delay in the solution finding a steady state. Cyclic voltammetry showed the polishing reaction to be irreversible with no affinity for the polished uranium species to redeposit on the working electrode once the potential has been swept back to the cathodic region. Instead, this region was dominated by the evolution of gas, likely to be H$_2$.

3.2. Chronoamperometry

A typical chronoamperometry curve is shown by the black line in Fig. 3. The same data is plotted against the square root of time (Cottrell plot) and on a logarithmic axis shown by the red and blue curves respectively. Initially, the current is high, close to 100 mA/cm^2. This regime continues until ~ 0.1 s, region 1, before the current decreases much more rapidly, achieving a new steady state that exists from between 1 - 20 s, region 2. The logarithmic curve, blue line, suggests a final regime which seems to only be emerging at times of beyond 200 s.
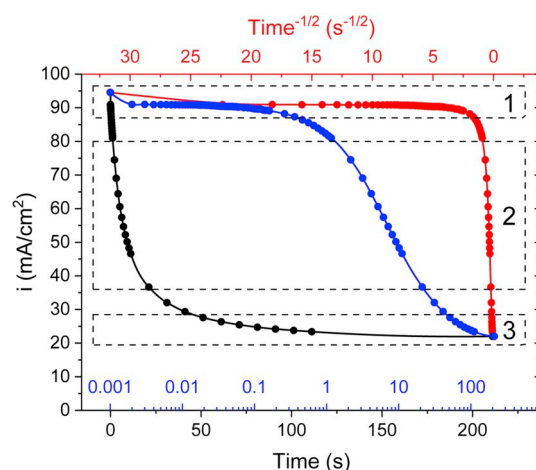

Fig. 3. Chronoamperometry plot showing the behaviour of the current with respect to time. The black curve is plotted on a linear axis, whereas the red curve shows a conventional Cottrell plot and the blue curve has been plotted with a logarithmic x axis. Each of these curves have been plotted to show the passage of time passing from left to right. (For interpretation of the references to colour in this figure legend, the reader is referred to the Web version of this article.)

Analysis of the gradients of the current on the Cottrell plot, red line, allows for assessment of the diffusion coefficients associated with each regime. Due to the relatively high uncertainty of some of the coefficients of Cottrell's equation [23], a better measure is the ratio between the two. The diffusion coefficient in region 1 was found to be $(1.0 \pm 0.3) \times 10^7$ times larger than that of region 2. It is thought that region 1 represents a transfer of charge through the layer initially adjacent to the working electrode surface, whereas region 2 relies on the diffusion of ions to the vicinity of the sample to continue the production of current. Region 3 could be arising from changing chemistry either in the bulk solution or due to the growth of a very thin oxide film. A slight orange tinge could be observed on the surface of samples that had experienced a significant amount of polishing time. It was observed that this thin oxide film (also observed by Angerman [24]) could be dissolved by maintaining the open circuit potential for a short time following polishing. All chronoamperometry test, as a result, culminated in at least a minute of 'rest' in which the oxide was allowed to dissolve.

3.3. Polishing potentials

To confirm the optimal polishing potential, five samples cut from the same batch were examined at varying potentials corresponding to unique points on the linear sweep curve, Fig. 2. Polishing time was kept fixed for all samples in this study at 210 s. The resultant EBSD maps are shown in Fig. 4. Average confidence index was observed to rise with increasing potential with a maximum at 4 V.

Fig. 4 appears to agree well with basic electropolishing theory [25]. Whilst the potential is less than the peak of the linear sweep curve, the polishing is poor and EBSD patterning is largely unsuccessful. Pore formation was additionally observed at low voltages which may have been contributing to poor patterns through a non-flat surface. It is assumed at these low potentials, the amount of material removed has been insufficient to allow sampling of material free from mechanical damage. As the potential rises and enters the plateau region, the polishing is more effective and confidence indices increase. Given a relatively short polishing time and originally rough surface, samples have quite varied CI's at this stage. There may also be issues with sample homogeneity. However, the 4.0 V and 7.0 V samples are indexing the entire sample effectively, and a potential in this range has proven to be effective in producing good EBSD maps. Chronoamperometry scans of the 5 test samples are shown in Fig. 5. All potentials representing stable
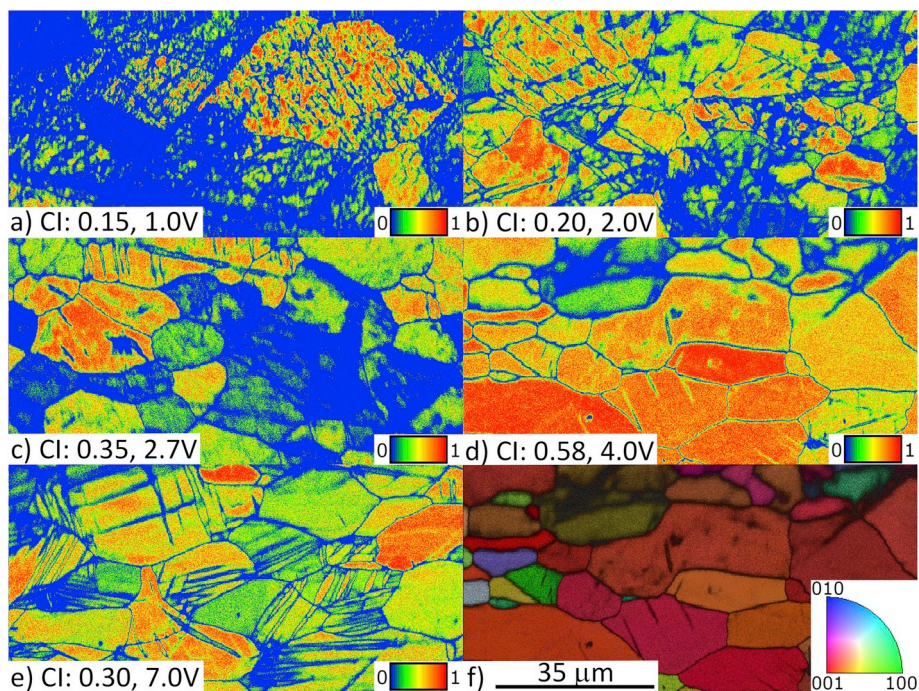
Fig. 4. a) - e) EBSD CI maps of samples which had experienced progressive polishing potentials (all for 210 s) measured with a step size of 0.1 μm. f) EBSD CI + IPF map of the best polished sample, d). Scale bar serves all maps which are 100 × 50 μm in size.
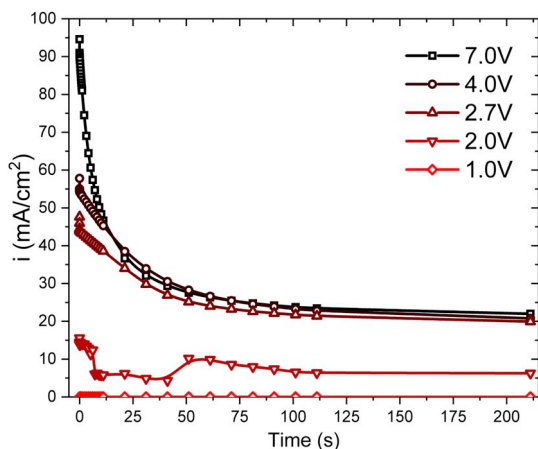

Fig. 5. Chronoamperometry scans pertaining to the 5 samples. As the potential of the choronoamperometry step is increased, the instantaneous current also increases. For higher potentials, steady-state current is limited at roughly 23 mA/cm^2. Potentials of 1.0 or 2.0 V were insufficient in producing reliable polishing. Data points have been joined up with spline curves to simply show the trends.

polishing were ultimately limited in current density at 20–25 mA/cm^2 at 210 s. 30 mA/cm^2 has been reported as optimal polishing conditions using a similar solution [24].

3.4. Polishing durations

Total polishing time was subsequently examined by varying polishing durations whilst maintaining the potential at 5.5 V, as was found to be within the suitable range of potentials in the previous section. Maps received from this study are shown in Fig. 6.

Though there appear to be slight differences in the microstructure, such as the prevalence for twinning, stronger patterns were achieved for longer polishing durations. Alternatively, deformation twinning may have been induced by mechanical preparation, but polishing has

removed sufficient material to observe mostly un-deformed material, as shown in images e and f. In addition to the polishing duration, it appears that grain orientation is strongly affecting the pattern certainty. The pair of images, e and f, show many grains have uniform confidence indices within a grain whereas their neighbours have a lower confidence that is also uniform within the grain. Reasons for this result may be due to the preference that a grain may have for electropolishing due to superior polishing rates [26], initial inherent oxide thickness or the number of lattice planes contributing to the scattering of electrons in each crystallographic orientation. There is also another effect relating to the density of Kikuchi bands crossing the detector screen given a grain's orientation [27].

Some papers have found that lengthy polishing time has the potential to roughen the surface after a point, subsequently reducing the pattern quality [28]. In this case, the polishing is occurring on a sufficiently slow scale and as the material possesses a single phase, this effect does not appear to be contributing. The surface has been made considerably smoother following the final mechanical polishing stage to enable the production of good EBSD patterns.

3.5. Evaluation of residual stresses

A final sample was prepared to measure residual stresses and record EBSD maps. Mechanical polishing was extended to 3 and 1 μm diamond pastes to ensure the surface was scratch free. The sample was subsequently electropolished for 600 s at 5.5 V. Fig. 7 shows an EBSD map of many grains including a clustering of carbide inclusions. Although most of the carbides have been stripped out in the polishing process, evidence of crystal structure remains in their pits and is capable of being indexed. Due to the shape of the carbide pits, only portions are flat and shallow enough to direct the electron beam to the detector to be indexed.

The reason for the preferential stripping of the carbides is unclear. With a lower conductivity than the metal, it might initially be assumed that the metal should be preferentially etched, ejecting the carbides. Alternatively, the heightened hardness of the carbides leads them to protrude the surface following mechanical polishing, causing them to
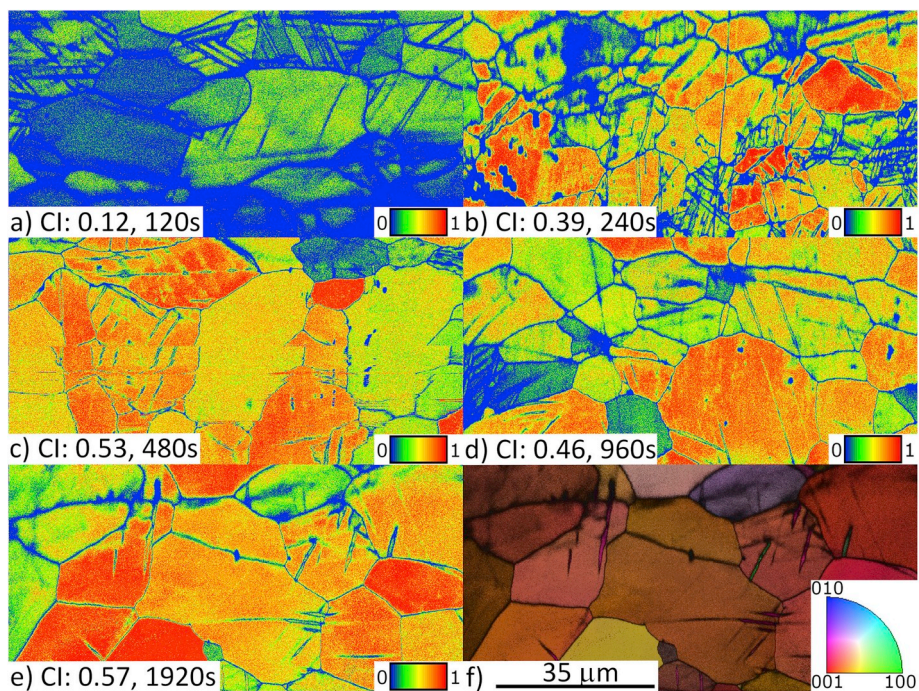
Fig. 6. a) - e) EBSD CI maps of samples which had experienced progressive polishing durations (all at 5.5 V) measured with a step size of 0.1 μm. f) EBSD CI + IPF map of the best polished sample, e). Scale bar serves all maps which are 100 × 50 μm in size. Beam drift in image c has resulted in a disjointed image.

disrupt the Helmholtz double layer and focus polishing in the vicinity. Pockets of higher contrast in Fig. 7 show regions where the confidence index was higher around ejected carbides. In these regions, quicker polishing of metal may have caused material behind the carbide to be polished much more quickly until they are ejected.

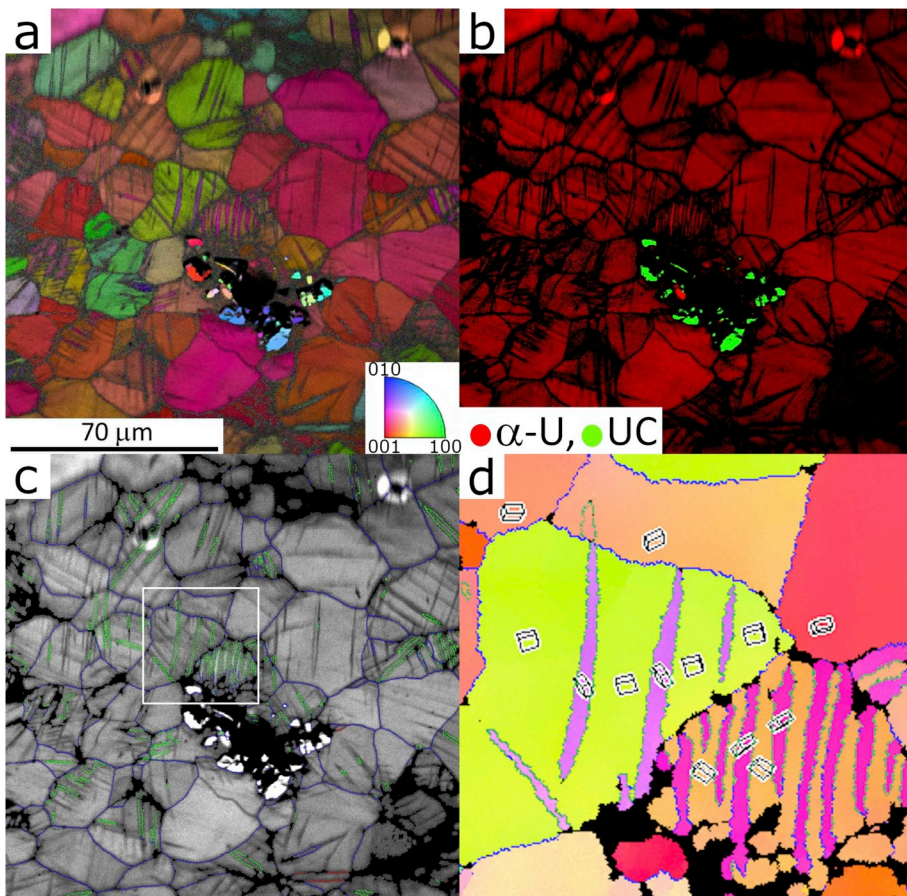Uranium possesses a large number of deformation mechanisms as a

Fig. 7. a) EBSD CI + IPF map of a pristinely finished sample measured with a step size of 0.2 μm. A large proportion of the sample was successfully indexed with primarily grain boundaries and crystallographic defects responsible for un-indexed regions. In the polishing process, a clustering of carbides was preferentially removed. In the resultant pit, portions were capable of being mapped with a UC material file. b) EBSD Phase map showing the distribution of the two phases. c) EBSD Image Quality (IQ) map marked up with identified {130} twin boundaries shown as green lines and {112} twin boundaries by red lines. Boundaries with rotation angles between 15 and 180° are shown by blue lines. d) EBSD IPF map showing a close up of the box shown in c) where the orientations of the crystal have been annotated. (For interpretation of the references to colour in this figure legend, the reader is referred to the Web version of this article.)
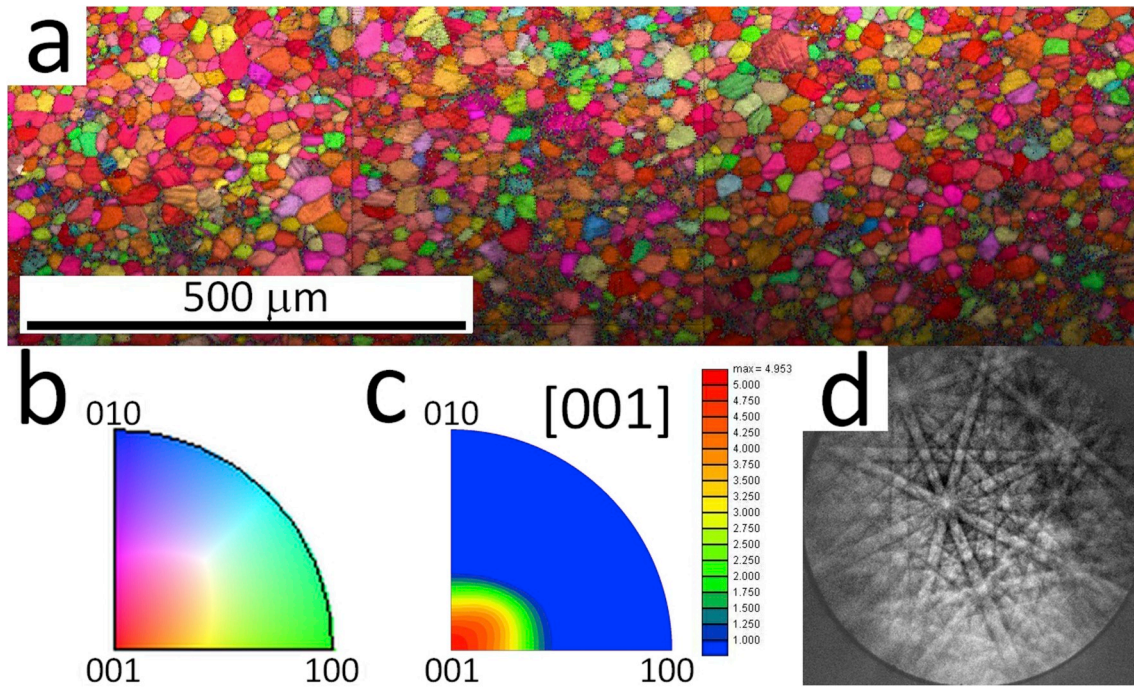
Fig. 8. a) Large EBSD IQ + IPF map measuring 1.5 × 0.5 mm measured with a step size of 1 µm. Due to the large region, the effect of sample tilt and low magnification acts to reduce the quality of focus (and therefore pattern quality) at the bottom of the image. b) Inverse Pole Figure map orientation legend. c) Unit stereographic triangle of the inverse pole figure texture plot oriented for the normal direction. d) Typical Kikuchi pattern obtained from the final sample in-focus. 1 × 1 binning was implemented with no background subtraction for this pattern to assess the feasibility of cross correlation EBSD.

result of its complex structure. Among these are Type I ({112} and {111}), Type II ({1 $\bar{7}$ 2}) and compound ({130} and {110}) twins, slip that acts predominantly in the [100] direction on the (010) plane, and kink bands approximately normal to the [100] direction [29,30]. In the best prepared sample, Fig. 7, substantial deformation to crystallites may be observed. The {130} twinning mode is particularly prevalent in the material matching literature observations [29,31,32]. Fig. 7 has also identified one example of a {112} twin but has failed to detect any of the other twins. It is expected that a higher resolution map would be required to identify these often finer twins. Most of the grains probed in this scan have returned a reasonable to good EBSD pattern leading to a broadly gaussian confidence index distribution with a mean of 0.36 and a standard deviation of 0.22. The effect of grain orientation is thought to be contributing to the substantial variation in confidence indices [27].

Large EBSD maps were also acquired from the same sample as shown in Fig. 8. Due to the larger step size required for this scale (covering over 1 mm × 0.5 mm), twins are not easily observed. The preferred orientation is noticeable in this map and the modelled inverse pole figure texture plot is inset. Due to the mechanical working of the material during the manufacturing process, grains are biased towards the [001] direction oriented normal to the surface.

X-ray diffraction data from the optimised sample are shown in Fig. 9 with a Rietveld refinement fitted powder profile. Crystallographic texture is clearly prevalent in this material when compared to a standard powder pattern. Intensities are much higher for (002) and (112) reflections and diminished for the (021) and (131) planes. This result mostly agrees with the Inverse Pole Figure obtained via EBSD analysis, inset of Fig. 8, apart from a slight underestimation for the (001) oriented grains. As fixed divergence slits were used for the collection of this data, irradiation length varies with angle (2θ). However, the area studied by XRD was between roughly 10 and 50 times that covered by EBSD.
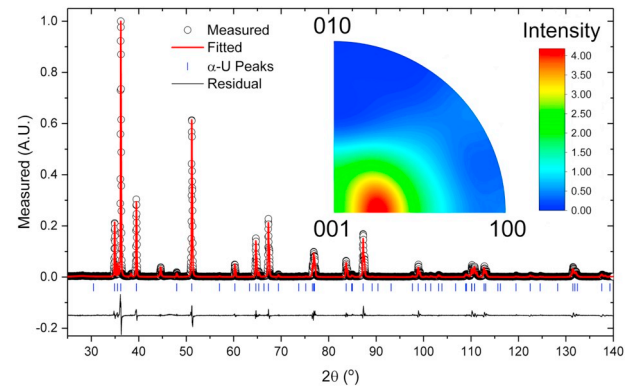

Fig. 9. Specular XRD scan fitted using Rietveld refinement. Inset shows an IPF representing the texture fit as a result of the refinement using spherical harmonics.

3.6. Williamson-Hall method

Williamson-Hall peak analysis was performed on the specular powder pattern to assess the material for strain. Peak widths were observed to increase at higher diffraction angles, as shown in Fig. 10. This small increase observed, $<1 \times 10^{-3}$, over such a large q range illustrates that there is little deviation in the periodic structure within the sampled volume. Using the formula,

$$\beta_{hkl} \cos\theta = \frac{K\lambda}{D} + \frac{\sigma_{hkl} \sin\theta}{E_{hkl}} \tag{2}$$

where β is the peak width, D is the particle size, K is Scherrer's constant and E_{hkl} is the in-plane elastic modulus, the average strain, $K\lambda/D$, and stress of each measured reflection, σ_{hkl}, can be assessed. In an orthorhombic system, such as uranium, E_{hkl} is given by,
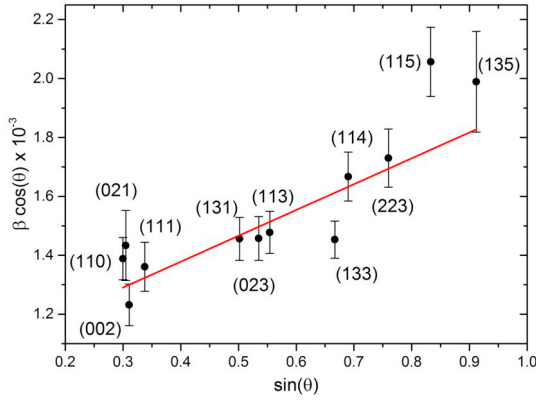
Fig. 10. Williamson-Hall plot of fitted uranium peaks from Fig. 9. The red line denotes a linear best fit with gradient of $(8.8 \pm 1.9) \times 10^{-4}$. A couple of outliers might indicate that the complex mechanical deformation pathways of uranium are affecting some planes greater than others. (For interpretation of the references to colour in this figure legend, the reader is referred to the Web version of this article.)

$$
\begin{aligned}
(E_{hkl})^{-1} &= n_1^4 s_{11} + n_2^4 s_{22} + n_3^4 s_{33} \\
&\quad + n_2^2 n_3^2 s_{44} + n_1^2 n_3^2 s_{55} + n_1^2 n_2^2 s_{66} \\
&\quad + 2n_1^2 n_2^2 s_{12} + 2n_1^2 n_3^2 s_{13} + 2n_2^2 n_3^2 s_{23}
\end{aligned}
\tag{3}
$$

where n_i are the Euler angles between reflections and the principal axes, s_{ij} are the inverse of the elastic stiffness moduli, c_{ij}, $(s_{ij} = c_{ij}^{-1})$ obtained from Fisher and McSkimin [33]. Using the in-plane elastic modulus produced a stress of -83 ± 33 MPa. In comparison, treating the material as having undergone uniform compressive stresses and possessing an elastic modulus of 201 GPa [34], a crude assessment of the stress may be evaluated as -45 ± 9 MPa. The reduced scatter of the fitted line and the resulting lower error suggests that this model of isotropic strain is the better one. However, the various deformation pathways of uranium, such as twinning and slip, have not been accounted for in this analysis.

3.7. Sin²ψ Method

Small shifts in peak positions were observed on the order of thousandths of Ångströms. For the high values of 2θ used, this approaches the resolution of the diffractometer. Peak shifts to higher values in 2θ, indicate decreasing interplanar distances arising from compressive stresses. This fits with the expectation that mechanical working compresses most crystal orientations.

Given the results from the last section, the bulk elastic modulus was used to determine the stress for each reflection using,

$$
\sigma_{hkl} = \frac{E}{1 + \nu} \frac{d\varepsilon}{d(sin^2\psi)}
\tag{4}
$$

where ν is Poisson's ratio for uranium, 0.23 [34], and ε is the strain between the ideal and measured peak position, based on a Rietveld fitting of the entire pattern. The stress can therefore be extracted from the gradients of the curves.

Fig. 11 shows the relationship between interplanar spacing and $sin^2\psi$. Under uniform stress, the relationship should be linear. The data in this experiment appears to be well described by parabolic curves, denoting an inhomogeneous stress profile that increases closer to the surface. To assess the stresses for each crystallographic direction, the fitted curves were differentiated analytically and evaluated at the highest available value of $sin^2\psi$. This gave an upper estimate of the stress for the material closest to the surface. Using the uniform stress deformation model, stresses were determined to be $\sigma_{115} = -841 \pm 156$ MPa and $\sigma_{135} = -815 \pm 168$ MPa. A value of $\sigma_{223} = -448 \pm 227$ MPa was produced for the (223) reflection but as values above
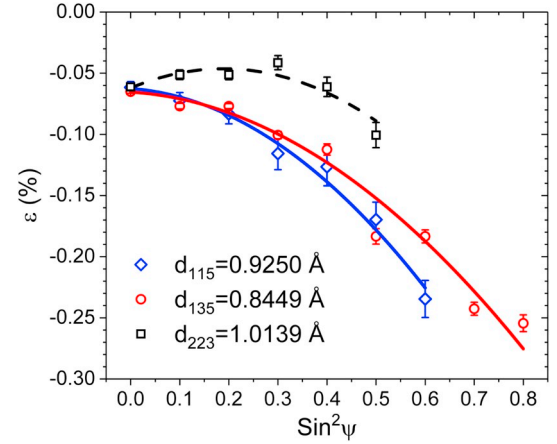

Fig. 11. $Sin^2\psi$ plot for three intense reflections at the higher end of uranium's XRD powder pattern. Reflections relating to smaller interatomic spacings permit the greatest tilting in the ω-axis mode, thereby allowing shallower measurements, see Equation (1).

$sin^2\psi = 0.5$ could not be accessed, fewer data points are available and the fit is less reliable. The stress evaluated at $sin^2\psi = 0$, where the same volume is sampled under the Williamson-Hall method, produces a consistent result (averaged -44 ± 44 MPa for the (115) and (135) reflections). As the compressive yield strength of uranium is roughly 750 MPa [14], only the top few layers could be slightly plastically compressed.

4. Discussion

Using a systematic approach, an appropriate polishing potential of at least 3 V has been found to be sufficient for this system. Potentials significantly less than 3 V has been shown to produce unsatisfactory results. This is possibly due to an inability to form a sufficiently strong double layer promoting consistent polishing. Whilst there was little difference above 3 V in terms of quality of EBSD patterns received, it is the authors' belief that oxide formation should be more prevalent over time and operating at higher voltages shows no gain in terms of quality of polish so should be discouraged. This work has highlighted that there is plenty of scope to expand, particularly using different solutions to gauge the effectiveness of each.

XRD investigations confirm the lack of oxide present on the sample and that the metal is highly textured. Peak profile analysis from the specular data using the Williamson-Hall method shows little strain throughout the metal. This is reinforced by the $sin^2\psi$ data illustrating that small strains and stresses are observed but increase towards the surface of the material. These two experiments show that the mechanical and electrical polishing undertaken has produced a low-strain surface, representative of bulk material. Alternative descriptions of non-linear $sin^2\psi$ plots include ψ-splitting behaviour resulting from shear stresses or textural effects [19]. It was not feasible to probe all these possibilities in this study. However, examination of this in uranium would be interesting in itself due to its complexity in crystallographic structure and deformation routes.

This low-stress surface is also evident through the quality of EBSD patterns measured from uranium, a high Z-material. Large areas accessible using this polishing procedure illustrate an ability to acquire information on the scale of millimetres, crucial for material characterisation and many real-world corrosion experiments. Mapping such large scales has allowed for the assessment of useful material characteristics such as grain size and texture.

Kikuchi patterns obtained in this study have enabled the interrogation of twin and carbide formation. The authors believe that the surface and pattern quality produced in uranium from this optimised

process are of a sufficiently high quality for Cross-Correlation EBSD [35–38], an example of a typical EBSD pattern is shown in Fig. 8. This would allow investigation of the origin of stresses within the material, which are likely to be focused around crystallographic defects such as twins and grain boundaries.

The influence of grain orientation is a large factor in the correct assignment of phases and could be assisted by further investigation. Given the low crystal symmetry, it would be reasonable to expect differences in image quality and therefore confidence index to arise from crystallographic orientation [39]. Since stresses are low and there is no obvious oxide present, the effect is expected to be due to crystallographic orientation.

5. Conclusions

This paper has illustrated that in uranium, production and characterisation of low-stress surfaces is possible using a relatively simple setup. In this case, optimal polishing potentials were found to occur beyond 3 V, with 5 - 10 min sufficient to produce good patterns from an initially quite rough surface. The work has shown development of the processes of electropolishing, enabling a standard protocol for the assessment of electropolishing procedures. Ultimately, a combination of mechanical and electrochemical surface preparation methods have been used to produce very uniform surfaces allowing for reliable mapping of large regions using EBSD. These maps have been successful in identifying the salient microstructural features such as grain boundaries, dominant twinning mechanisms (primarily {130} twins) and inclusions. It is key to illustrate that the resultant surface and strain state produced is not a result of the preparation method, but representative of bulk material. Therefore, this method can be utilised as a tool for interrogating microstructures as well as acting as a model start point for corrosion or oxidation experiments.

Data availability

The raw data that support the findings of this study may be available on request by contacting the corresponding author. Restrictions apply to the availability of these data. Sharing data may be possible with the permission of AWE plc.

Declaration of competing interest

The authors declare that they have no known competing financial interests or personal relationships that could have appeared to influence the work reported in this paper.

Acknowledgements

References

[1] R.J. McCabe, D.F. Teter, Analysis of recrystallized volume fractions in uranium using electron backscatter diffraction, J. Microsc. 223 (1) (2006) 33–39, https://doi.org/10.1111/j.1365-2818.2006.01595.x.

[2] M.M. Nowell, R.A. Witt, B.W. True, EBSD sample preparation: techniques, tips, and tricks, Microscopy Today 13 (4) (2005) 44–49.

[3] A.M. Kelly, D.J. Thoma, R.D. Field, P.S. Dunn, D.F. Teter, Metallographic preparation techniques for uranium, J. Nucl. Mater. 353 (3) (2006) 158–166, https://doi.org/10.1016/j.jnucmat.2005.12.008.

[4] A. Kelly, D. Thoma, R. Field, E. Cerreta, R. Hackenberg, Metallographic preparation techniques for uranium/uranium alloys, Microsc. Microanal. 18 (S2) (2012) 454–455, https://doi.org/10.1017/S1431927612004126 URL http://www.journals.cambridge.org/abstract_S1431927612004126.

[5] T.B. Scott, J.R. Petheridge, I. Findlay, J. Glascott, G.C. Allen, Recrystallisation of

[6] uranium resulting from electron beam welding, J. Alloy. Comp. 475 (1–2) (2009) 766–772.

[6] D.A. Carpenter, R.L. Bridges, Surface preparation of uranium by ion milling, Microscopy Today 16 (3) (2008) 28–31.

[7] T. Ajantiwalay, T. Trowbridge, A. Winston, C. Sun, K. Sridharan, A. Aitkaliyeva, Best practices for preparing radioactive specimens for EBSD analysis, Micron 118 (2019) 1–8.

[8] X. Iltis, I. Zacharie-Aubrun, H.J. Ryu, J.M. Park, A. Leenaers, A.M. Yacout, D.D. Keiser, F. Vanni, B. Stepnik, T. Blay, Microstructure of as atomized and annealed U-Mo7 particles: a SEM/EBSD study of grain growth, J. Nucl. Mater. 495 (2017) 249–266.

[9] D. Jadernas, J. Gan, D. Keiser, J. Madden, M. Bachhav, J.-F. Jue, A. Robinson, Microstructural characterization of as-fabricated and irradiated U-Mo fuel using SEM/EBSD, J. Nucl. Mater. 509 (2018) 1–8.

[10] J.F. Bingert, R.J. Hanrahan Jr., R.D. Field, P.O. Dickerson, Microtextural investigation of hydrided α-uranium, J. Alloy. Comp. 365 (1–2) (2004) 138–148.

[11] W. Xu, M. Ferry, N. Mateescu, J.M. Cairney, F.J. Humphreys, Techniques for generating 3-D EBSD microstructures by FIB tomography, Mater. Char. 58 (10) (2007) 961–967.

[12] G.D. West, R.C. Thomson, Combined EBSD/EDS tomography in a dual-beam FIB/FEG–SEM, J. Microsc. 233 (3) (2009) 442–450.

[13] K.E. Knipling, D.J. Rowenhorst, R.W. Fonda, G. Spanos, Effects of focused ion beam milling on austenite stability in ferrous alloys, Mater. Char. 61 (1) (2010) 1–6.

[14] V. Yemel'Yanov, A. Yevstyukhin, The Metallurgy of Nuclear Fuel, Pergamon Press Ltd., 1969.

[15] C.L. Angerman, R.T. Huntoon, Network structures in uranium and its alloys, J. Less Common Met. 9 (5) (1965) 338–353.

[16] V. ASM, International Handbook, Properties and selection: nonferrous alloys and special-purpose materials, ASM Metals Handbook 2 (1990) 1300, https://doi.org/10.1016/S0026-0576(03)90166-8.

[17] S.I. Wright, M.M. Nowell, S.P. Lindeman, P.P. Camus, M. De Graef, M.A. Jackson, Introduction and comparison of new EBSD post-processing methodologies, Ultramicroscopy 159 (2015) 81–94.

[18] G.K. Williamson, W.H. Hall, X-ray line broadening from filed aluminium and wolfram, Acta Metall. 1 (1) (1953) 22–31.

[19] U. Welzel, J. Ligot, P. Lamparter, A.C. Vermeulen, E.J. Mittemeijer, Stress analysis of polycrystalline thin films and surface regions by X-ray diffraction, J. Appl. Crystallogr. 38 (2005) 1–29, https://doi.org/10.1107/S0021889804029516.

[20] NIST, Physical Measurement Laboratory, X-ray mass attenuation coefficients, URL https://physics.nist.gov/PhysRefData/XrayMassCoef/ElemTab/z92.html.

[21] A.P. Hammersley, C. Riekel, MFIT: multiple spectra fitting program, Synchrotron Radiat. News 2 (1) (1989) 24–26.

[22] B. Toby, R. Von Dreele, GSAS-II: the genesis of a modern open-source all purpose crystallography software package, J. Appl. Crystallogr. 46 (2013) 544–549.

[23] F.G. Cottrell, Der Reststrom bei galvanischer Polarisation, betrachtet als ein Diffusionsproblem, Z. Phys. Chem. 42 (1) (1903) 385–431.

[24] C.L. Angerman, Transmission electron microscopy of uranium, J. Nucl. Mater. 9 (1) (1963) 109–110.

[25] C. Wagner, Contribution to the theory of electropolishing, J. Electrochem. Soc. 101 (5) (1954) 225–228.

[26] N.W. Khun, M. Sumption, G.S. Frankel, Smoothening of niobium by electropolishing, J. Appl. Electrochem. 43 (8) (2013) 829–838.

[27] M.M. Nowell, S.I. Wright, Orientation effects on indexing of electron backscatter diffraction patterns, Ultramicroscopy 103 (1) (2005) 41–58.

[28] C. Rotty, A. Mandroyan, M.-L. Doche, J.Y. Hihn, Electropolishing of CuZn brasses and 316L stainless steels: influence of alloy composition or preparation process (ALM vs. standard method), Surf. Coat. Technol. 307 (2016) 125–135.

[29] R. Cahn, Plastic deformation of alpha-uranium; twinning and slip, Acta Metall. 1 (1) (1953) 49–70, https://doi.org/10.1016/0001-6160(53)90009-1.

[30] G.H. Lander, E.S. Fisher, S.D. Bader, The solid-state properties of uranium A historical perspective and review, Adv. Phys. 43 (1) (1994) 1–111, https://doi.org/10.1080/00018739400101465.

[31] P. Zhou, D. Xiao, W. Wang, G. Sang, Y. Zhao, D. Zou, L. He, Twinning behavior of polycrystalline alpha-uranium under quasi static compression, J. Nucl. Mater. 478 (2016) 83–90.

[32] L.T. Lloyd, H.H. Chiswik, Deformation mechanisms of alpha-uranium single crystals, J. Occup. Med. 7 (11) (1955) 1206–1214.

[33] E.S. Fisher, H.J. McSkimin, Adiabatic elastic moduli of single crystal alpha-uranium, J. Appl. Phys. 29 (10) (1958) 1473–1484.

[34] P.E. Armstrong, D.T. Eash, J.E. Hockett, Elastic moduli of alpha, beta and gamma polycrystalline uranium, J. Nucl. Mater. 45 (3) (1972) 211–216.

[35] A.J. Wilkinson, Measurement of elastic strains and small lattice rotations using electron back scatter diffraction, Ultramicroscopy 62 (4) (1996) 237–247.

[36] A.J. Wilkinson, T.B. Britton, Strains, planes, and EBSD in materials science, Mater. Today 15 (9) (2012) 366–376.

[37] T.B. Britton, S. Birosca, M. Preuss, A.J. Wilkinson, Electron backscatter diffraction study of dislocation content of a macrozone in hot-rolled Ti–6Al–4V alloy, Scr. Mater. 62 (9) (2010) 639–642.

[38] M. Ojima, Y. Adachi, S. Suzuki, Y. Tomota, Stress partitioning behavior in an fcc alloy evaluated by the in situ/ex situ EBSD-Wilkinson method, Acta Mater. 59 (10) (2011) 4177–4185.

[39] S.I. Wright, M.M. Nowell, EBSD image quality mapping, Microsc. Microanal. 12 (1) (2006) 72–84.